# Monolithic Carbons with Tailored Crystallinity and Porous Structure as Lithium-Ion Anodes for Fundamental Understanding Their Rate Performance and Cycle Stability

Guang-Ping Hao, Fei Han, De-Cai Guo, Rui-Jun Fan, Guang Xiong, Wen-Cui Li,* and An-Hui Lu*

State Key Laboratory of Fine Chemicals, School of Chemical Engineering, Faculty of Chemical, Environmental and Biological Science and Technology, Dalian University of Technology, Dalian 116024, P. R. China

Ⓢ Supporting Information

ABSTRACT: A series of hierarchically multimodal (micro-, meso-/macro-) porous carbon monoliths with tunable crystallinity and architecture have been designedly prepared through a simple and effective gelation through a dual phase separation process and subsequent pyrolysis. Because of the magnificent structural characteristics, such as highly interconnected three-dimensional (3D) crystalline carbon framework with hierarchical pore channels, which ensure a fast electron transfer network and lithium-ion transport, the carbon anodes exhibit a good cycle performance and rate capability in lithium-ion cells. Importantly, a correlation between the electrochemical performances and their structural features of crystalline and textural parameters has been established for the first time, which may be of valid for better understanding of their rate performance and cycle stability.
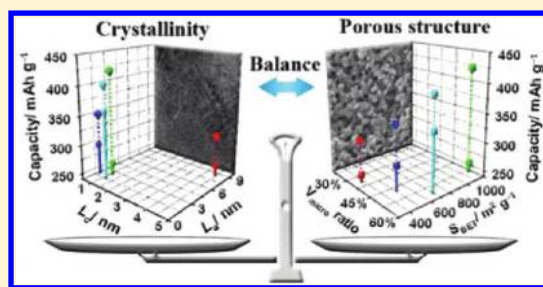
INTRODUCTION

Lithium-ion rechargeable batteries (LIBs) have been popularly used for portable electronics.[1−3] However, the issue arising from the low charge/discharge rate and unstable cycle performance of LIBs continue to plague their potential application in large-scale energy storage devices (e.g., electric vehicle).[4−6] The key to address the problems lies in designing advanced materials with fast charge−discharge capability and high cycle stability. Currently, carbonaceous materials are the mainstay of anode materials in practical LIBs. Among them, graphite is considered the state-of-the-art anode material, mainly due to its high reversibility and low operating potential.[7−9] However, graphite anodes exhibit mediocre charge/discharge rate performance because of the slow diffusion of lithium ions in the well-packed layers of hexagonally arranged carbon atoms. Moreover, the lack of active surface area and porosity aggravates this issue. Carbon nanotubes (CNTs) are another kind of graphitic carbon but present increased topological defects, which account for a high lithium insertion capacity. Despite the lithium-ion storage capacities, the applicability of CNTs in practical LIBs is hampered by their large first-cycle irreversible capacities and the large hysteresis between the charge−discharge potentials.[10] On the other hand, amorphous carbons featured by a predominance of single, unaligned and buckled carbon layers as well as a variety of pores in nanometer scale also provide abundant sites for lithium accommodation.[11] Similar to CNTs, they exhibit large irreversible capacities. Moreover, their electronic conductivity is also inferior to that of well crystalline graphite or CNTs. Considering the main factors aforementioned, an anticipated electrode material should integrate the features of

high electronic conductivity, rapid ion transport (short diffusion distance and low inner-pore ion-transport resistance), and moderate active sites for reversible intercalation of lithium ion.

Crystalline pore wall is effective to achieve a high electronic conductivity. However, the transformation to crystalline phase (graphitization) generally leads to a poorly developed porosity, which reduces the electrode/electrolyte interface and thus limits the charge-transfer reaction process.[12−14] Carbon electrodes with a high surface area are generally capable of a high contacting efficiency between the electrode and electrolyte by facilitating the Li-ion exchange across the electrode/electrolyte interface. However, the inherently increased amount of defects (e.g., vacancies, boundaries, edges, and corners) usually lead to a sharp accumulation of irreversible capacities because of the strong trapping of the guest lithium ions. Therefore, trade-offs between the crystallinity and the amount of active sites must be carefully examined. As an example, the work by Su et al. revealed that a graphitic pore wall of a highly porous carbon delivered a much better reversible capacity and rate performance than its amorphous counterpart.[15]

As proposed by Goodenough and co-workers, at a high current density, the ionic motion (chemical diffusion of lithium ion) across the electrode/electrolyte interface is much slower than the electron transport in the external circuit. Consequently, it fails to reach charge equilibrium and consequently leads to a high irreversible capacity.[5] To mitigate this imbalance, the electronic current density, in most cases it

prevails, should match the internal ionic current density, i.e., the rate-limiting step, as closely as possible. Kinetically, graphitic carbon hosts with a hierarchical pore architecture combining interconnected pores at the nanometer and micrometer scales allow a high electrochemically active surface area, a fast flow rate of the electrolyte fluids as well as a short grain boundary by 3D conducting carbon branches in a limited space.[16−18] Zhou et al. have employed the amorphous carbon nanostructure with 3D hexagonal pore channels as an anode, which delivered a very high reversible capacity of 850−1100 mA h g^{-1} in 20 cycles at a current of 100 mA g^{-1}.[19] Later, Hu et al. demonstrated a nanocast carbon monolith as anode material with significantly hierarchical meso-/macroporosity showed superior high-rate performance. 3D ordered macroporous carbon (3DOM) with abundant macropores and micropores is also tested as anode electrode.[20] However, due to the excess voids in micrometer scale but the lack of pores with size in mesoscale, the 3DOMs often suffer from low capacity and volumetric energy density. One step further, Fang et al. recently developed an ordered multimodal porous carbon (OMPC) anode that composed of a well-developed 3D interconnected ordered macropore framework with open mesopores embedded in the macropore walls.[17] Remarkably improved reversible capacity with the unprecedented value of 799 mA h g^{-1} (100 mA g^{-1}, 80 circles) was obtained, which is even higher than the sum of that of the ordered mesoporous carbon (ca. 500 mA h g^{-1}) and the ordered macroporous 3DOM (ca. 200 mA h g^{-1}).[21] This indicates the synergistic effect of the mesopores and macropores for high rapid ion transport and reversible storage.[22]

Clearly, the exploitation for high-performance LIBs exhibiting better rate capability and higher cycle stability to power a large-scale energy storage electronic device still continues.[23−26] Nevertheless, a few works have paid attention to figure out the correlation of the crystallinity and architectures vs its electrochemical performances of an electrode material, though they reported sound synthesis and/or electrochemical results.[27−31] It is thus of importance to fundamentally understand the internal relation between the pore features of a porous carbon anode and the rate performance and cycle stability. To complete the association on a comparable basis, it is better to use control samples that are derived from the same precursors and are structurally tailorable. The reported products, which mainly prepared through either high-temperature graphitization or catalytic graphitization, are quite monotonous in structural properties (less developed porosity and high crystallinity). In this study, we have purposively synthesized hierarchically multimodal (micro-, meso-/macro) porous carbons with tunable graphitization degree and surface areas and then further associated their electrochemical performance as an anode of LIBs with their structural features of crystalline and textural parameters.

■ EXPERIMENTAL SECTION

Synthesis of Graphitic Carbon Nanostructures. The carbon precursors were prepared by the polymerization of resorcinol with formaldehyde (denoted RF) in the presence of a catalyst complex of L-glutamic acid (denoted GLU) and ferric trichloride. For a typical synthesis, 1.50 g of resorcinol was dissolved in 2.21 g of formaldehyde aqueous solution (37 wt %) under magnetic stirring to get a homogeneous prepolymer solution A. Meanwhile, 0.80 g of GLU and 1.00 g of FeCl$_3$·6H$_2$O were added to 1.93 mL of deionized water

under vigorous magnetic stirring to form homogeneously orange and transparent solution B within 5 min. Then, solution B was poured into solution A under magnetic stirring, and very quickly (in 1 min) the mixed solution turned to homogeneously deep black and opaque in color. After stopping stirring, the gloomy wet gel was rapidly formed in a couple of minutes at room temperature. The gels were cured at 50 °C for 10 h and then 90 °C for 10 h, followed by ambient pressure drying at 50 °C for 24 h. The dried polymer was heated to 800 °C and held at that temperature for 2 h in a tube furnace under nitrogen to obtain the carbon composite materials. After removal of the ferric species by acid leaching, graphitic carbon was obtained, which was denoted RFG-1. Carbon sample (denote RFG-2) with improved nanoporosity was prepared by steam activation of RFG-1 (1.50 g) at 850 °C for 20 min. In order to synthesize more amorphous carbon (denote RFG-3), carbon precursor was first treated with acid to remove ferric species and then pyrolyzed under N$_2$ flow at 800 °C for 2 h. In this case, RFG-3 with similar macroporosity as RFG-1 and RFG-2 was obtained. Samples (denote RFG-4) with more developed porosity can be obtained by adding an additional 4.94 mL of water in solution A while retaining the other conditions identical to that of RFG-1. In all the syntheses, the molar ratio between resorcinol and formaldehyde was maintained at 1:2.

Characterizations. Raman spectra were collected on a homemade DL-2 microscopic Raman spectrometer, using a 244 or 532 nm line of a KIMMON laser. An Acton triple monochromator was used as a spectrometer for Raman scattering. The spectra were collected by a Prinston CCD detector. The experimental data detected by Raman spectra were fitted a least-squares function using the commercial software Origin 7.5. Values of the band position were derived from the result of the curve-fitting exercise. The X-ray diffraction (XRD) measurements were taken on a Rigaku D/Max 2400 diffractometer using Cu Kα radiation (40 kV, 100 mA, λ = 1.5406 Å). Scanning electron microscope (SEM) investigations were carried out with a Hitachi S-4800I instrument at 10 kV. TEM images were obtained with a FEI Technai F30 or a Hitachi HF2000 transmission electron microscope, equipped with a cold field emission gun. Samples were prepared by dropping a few drops of a suspension of a sample in ethanol onto the holey carbon grid with a pipet. Nitrogen sorption isotherms were measured with a Micromeritics tristar 3000 instrument at liquid nitrogen temperature. Samples were degassed at 200 °C for at least 4 h prior to determination of the isotherms. The Brunauer−Emmett−Teller (BET) method was utilized to calculate the specific surface areas (S_{BET}). Pore size distributions (PSDs) were derived from the adsorption branches of the isotherms using the Barrett−Joyner−Halenda (BJH) model. Micropore volumes (V_{micro}) were calculated using the t-plot method. Total pore volumes (V_{total}) were calculated at a relative pressure, P/P_0, of 0.97. Elemental analysis was carried out on a CHNO elemental analyzer (Vario EL III, Elementar). The Boehm titration method was used to determine the number of the oxygenated surface groups (see Supporting Information for details).

Electrochemical Test. The active material (80 wt %), conductive carbon black (10 wt %), and LA133 (10 wt %, water-based binder, Indigo) in water were mixed into a homogeneous slurry. The obtained slurry was pasted on rough copper foil to prepare the electrode film and followed by

dehydration at 100 °C for overnight in vacuum oven. Electrochemical measurements were carried out via CR2025 coin-type cell with lithium metal as the counter/reference electrode and Celgard 2400 membrane as the separator. The electrolyte was 1 M $LiPF_6$ dissolved in a mixture of dimethyl carbonate (DMC), ethyl methyl carbonate (EMC), and ethylene carbonate (EC) (1:1:1 v/v/v) with 2 wt % fluorinated ethylene carbonate (FEC) as an additive. The cells were assembled in an argon-filled glovebox with water and oxygen under 1 ppm. Galvanostatic charge−discharge cycles were tested by a LAND CT2001A electrochemical workstation at various current densities of 100−1000 mA g^{-1} between 0.005 and 3 V vs Li$^+$/Li at room temperature. EIS measurements were carried out before charge−discharge cycles in the frequency range of 100 kHz to 0.01 Hz with a zero-bias potential and 5 mV of amplitude.

■ RESULTS AND DISCUSSION

Hierarchically Porous Carbon Nanostructures with Controlled Crystallinity. Based on coordination chemistry, ferric iron attaches to both the amino acid and resorcinol by formation of coordinate bonds;[32] by that way the graphitization catalysts can be introduced in the sol and end up uniformly dispersion in the gel. It thus leads to the maximum contribution in crystalline phase transition during carbonization. Here, we harness this strategy, together with polycondensation and phase separation process, to synthesize the hierarchically multimodal (micro-, meso-/macro) porous carbon nanostructures with tunable graphitization features. The crystalline features of the obtained carbons (RFG-1 to RFG-4) were first evaluated by XRD techniques and Raman spectroscopy. The average crystallite size in the a-axis direction (L_a) of a graphene plane and the average crystallite size in the c-axis (L_c) are the most important two parameters that reflect the properties of graphitic carbons.[33] Figure 1a shows the wide-angle XRD
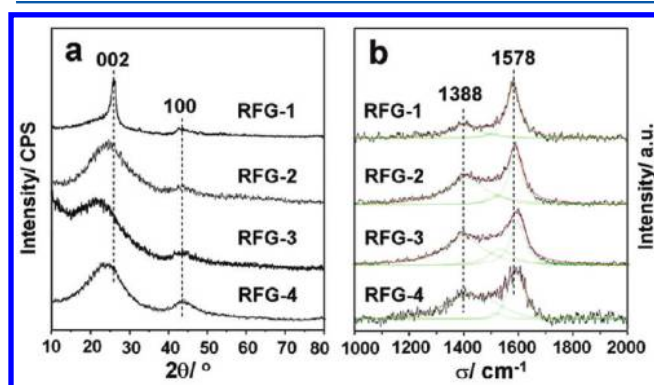

Figure 1. (a) Powder XRD patterns in the wide-angle region. (b) Raman spectra for RFG-1, RFG-2, RFG-3, and RFG-4.

patterns for RFG-1 to RFG-4. RFG-1 exhibits a strong peak located at 26.2° and a visible peak at 43.2°, which attributed to the planes (002) and (100), respectively. While the relatively wide (002) peaks of RFG-2 to RFG-4 are located at 2θ of 24.5°, 22.3°, and 24.2°, which evidence an lower order crystallinity.[34,35] According to Bragg's law, the interplanar spacing (d_{002}) is given by eq 1:[33]

$$d_{002} = \frac{\lambda}{2\sin\theta} \tag{1}$$

where λ is the wavelength of the incident X-ray beam and the copper Kα line is 1.5406 Å The calculated interplanar d spacing is 3.39, 3.63, 3.99, and 3.68 Å for RFG-1 to RFG-4, respectively. (It should be noted that 3.44 Å represents a certain specific structure of nongraphitized carbon according to Franklin model, i.e., the turbostratic structure put forward by Warren and co-workers. Because of such a restriction, in fact, sometimes the apparent interlayer spacing of the graphitic nanostructure is greater than 3.44 Å.[36−39]) These data reveal the interplanar d spacing for the nanostructured graphitic carbons is larger than that of bulk graphite due to short-range ordered domains. It is also clear that these nanostructures of RFG-1 to RFG-4 are varied in the graphitic degree.

In addition to the angle position, the width of the (002) peak is used to estimate the average graphite grain size by the Debye−Sherrer eqs 2 and 3:[33,39]

$$L_c = \frac{k\lambda}{B\cos\theta} \tag{2}$$

$$L_a = \frac{1.84k\lambda}{B\cos\theta} \tag{3}$$

where k is the shape factor (the value of 0.9), B is the line broadening at half the maximum intensity, θ is the Bragg angle, and λ is the wavelength of the X-rays.[40] The calculated values, L_c and L_a, are listed in Table 1. It was found that, among the four samples, RFG-1 shows the largest grain size with L_c of 4.5 nm and L_a of 8.3 nm, whereas the grain size of RFG-3 is the smallest with L_c of 0.8 nm and L_a of 1.5 nm. RFG-2 (L_c of 1.2 nm and L_a of 2.2 nm) and RFG-4 (L_c of 1.0 nm and L_a of 1.8 nm) show the moderate grain size, which is smaller than RFG-1 but larger than RFG-3.

Raman spectroscopy is a valuable method for the determination of bonding configuration of sp^2-hybridized carbon atoms. For bulk graphites, the Raman spectra show a strong, narrow peak at ca. 1548 cm^{-1} (G line), whereas the amorphous carbons usually give a strong peak at ca. 1354 cm^{-1} (D line).[35] Both peaks may broaden and shift to a higher or lower wavelength depending on the crystallinity changes of a specific carbon sample. In this work, two type lasers (244 and 532 nm) were employed to complete the Raman spectra. When using 532 nm laser line, the collected signals are very weak (see the Supporting Information, Figure S1) due to the extensive adsorption of the visible light by highly developed porosities of the porous carbons. Therefore, in the following, 244 nm line of laser was used to conduct the Raman spectra test and to calculate the relevant parameters based on the results. Figure 1b shows the Raman spectra for the four samples. As can be seen, besides G peak at 1578 cm^{-1}, all the four samples show an additional D line at 1388 cm^{-1}, which was ascribed to structural disorder. The relative intensity (R) of the two Raman lines (I_{1388}/I_{1578}) was found to depend upon the physical state of the graphitic carbon and reflects the graphitization degree. According to the established line shape analysis method,[41] the relative intensity of Raman lines (I_{1388}, I_{1578}) was the integrated intensity (area), and the spectra region of 1800−1200 cm^{-1} were fitted using a least-squares method taking three peaks into account. The R values for RFG-1 to RFG-4 were calculated to be 0.57, 1.47, 1.69, and 1.63 (shown in Table 1), respectively. This reveals that RFG-1 possesses the highest graphitization degree, while the crystallinity of RFG-3 is the poorest. The observation detected by Raman spectra are well in agreement with the findings by the XRD analysis. The average

Table 1. Physical and Chemical Properties of the Carbon Nanostructures

	porous textual parameters				crystalline index			overall composition (wt %)[h]				$O_{surface}$ (wt %)[j]	$O_{surface}/O_{overall}$[k] (%)
sample	S_{BET} $(m^2\ g^{-1})$[a]	V_{total} $(cm^3\ g^{-1})$[b]	V_{micro} $(cm^3\ g^{-1})$[c]	D_{ave} (nm)[d]	L_c (nm)[e]	L_a (nm)[f]	$R = (I_D/I_G)$[g]	C	H	N	O[i]		
RFG-1	371	0.31	0.11	3.39	4.5	8.3	0.57	81.22	1.11	0.70	14.26	0.919	6.44
RFG-2	1164	0.77	0.31	2.65	1.2	2.2	1.47	94.63	0.54	0.48	2.80	0.779	27.8
RFG-3	496	0.35	0.17	2.85	0.8	1.5	1.69	90.27	0.95	0.87	4.71	0.145	3.08
RFG-4	687	0.40	0.23	2.31	1.0	1.8	1.63	85.35	1.37	0.86	11.45	0.655	5.72

[a]Specific surface area calculated using the BET equation in the relative pressure range of 0.05−0.25. [b]Single point pore volume from adsorption isotherms at P/P_0 = 0.97. [c]Micropore volume calculated using the *t*-plot method. [d]The average pore size determined by N_2 adsorption data. [e]The average crystallite size in the *c*-axis direction calculated by using XRD data. [f]The average crystallite size in the *a*-axis direction calculated by using XRD data. [g]The ratio (R) of integrated intensity of the D line (I_D) to that of G line (I_G) calculated by Raman spectra. [h]The C, H, N content was directly detected by the elemental analysis. [i]Calculated by difference. [j]Surface oxygen content determined by Boehm titration (details see Table S2). [k]The percentage of the surface oxygen content to the overall oxygen content of the carbon nanostructures.

crystallite size L_a can be calculated using Tuinstra's eq 4 with Raman data:[33]

$$L_a = \frac{4.4}{I_{1388}/I_{1578}} \tag{4}$$

where I_{1388} and I_{1578} are the integrated intensities (area) of the 1388 and 1578 cm^{-1} bands, respectively. The determined L_a is 7.7, 3.0, 2.6, and 2.7 nm for RFG-1 to RFG-4, respectively. The difference of the calculated L_a between XRD (8.3, 2.2, 1.5, and 1.8 nm) and Raman techniques may arise from the different measurements. Combining the above results, it is clear that the formation of graphitic structures with controlled crystalline degree can be fabricated by our simple and effective methods.

The crystalline features and pore structures were further observed by TEM. As shown in Figure 2a,b, RFG-1 consists of well-developed nanosized graphitic domains. The thin graphitic shells and capsules that derived from the leaching of the ferric oxide can be clearly seen from Figure 2a, while the high-resolution TEM image (Figure 2b) shows the nanosized graphite belts and graphene nanoribbons, indicating its good crystallinity. As can be seen from Figure 2c,d, besides the
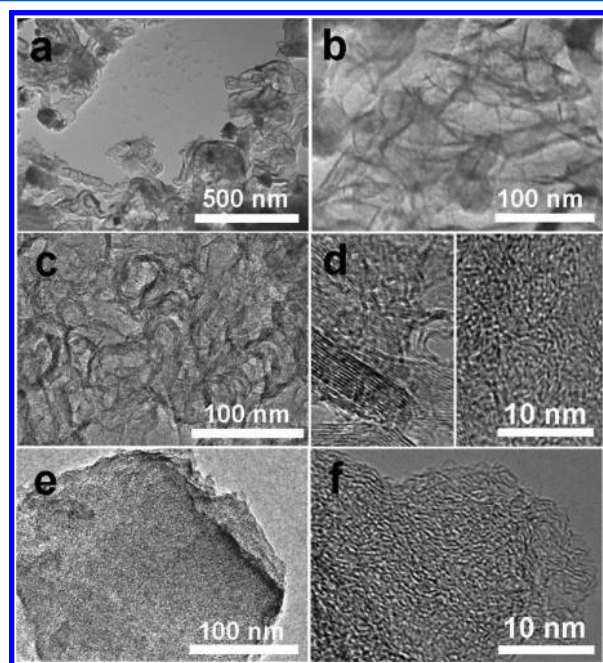
nanosized the turbostratic graphite belts, the nanostructure of RFG-2 contains rich micropores which arise from the extensive etching by water molecules during the activation process. The TEM image in Figure 2e shows dominating amorphous feature of RFG-4. The high-resolution TEM image of RFG-4 in Figure 2f clearly reveals the fully developed microporosities and partly turbostratic graphite structures. Hence, the TEM observation is in good agreement with the above XRD and Raman results.

In general, graphitization of amorphous carbon leads to a less developed porosity. To determine the pore parameters of these carbons, we conducted N_2 sorption measurements. The nitrogen sorption isotherms of RFG-1 to RFG-4 are shown in Figure 3a,b, and the textural parameters (S_{BET} and V_{total}) are
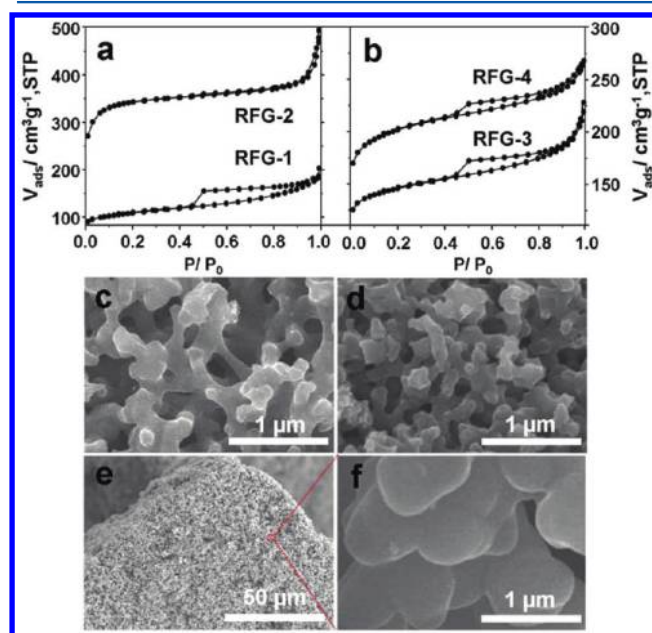

Figure 3. (a, b) N_2 sorption isotherms for RFG-1, RFG-2, RFG-3, and RFG-4; the SEM images for RFG-1 (c), RFG-3 (d), and RFG-4 (e and f with low and high resolution).

Figure 2. TEM images of RFG-1 (a, b), RFG-2 (c, d), and RFG-4 (e, f).

listed in Table 1. Their isotherms, except for RFG-2, show type IV characteristic with a clear hysteresis loop in the relative pressure range of 0.4−0.8, indicating the mesoporous characteristics, while a sharp increase of the adsorption quantity at a relative pressure near to 1.0, revealing the existence of macropores in the carbon nanostructures, particularly for RFG-2, RFG-3, and RFG-4. As shown, the most crystalline sample (RFG-1) exhibits much less porosity. However, this

poorly developed porosity can be improved by steam activation as demonstrated by the remarkable nitrogen uptake in the isotherm of RFG-2. The formation of the micropores etched by water molecules was confirmed by the TEM observation. The Raman and XRD analyses also reveal the extensive damage of the graphitic domains during steam activation process. For RFG-4, its highly developed micromesoporosity are exactly arising from the long-range randomly arrangement of the primary carbon fragments, which may account for the increased active sites. The S_{BET} and V_{total} are high with values of 687 m^2 g^{-1} and 0.40 cm^{3}g^{-1}, respectively, which further confirm its lower crystalline features.

The SEM images of RFG-1, RFG-2, and RFG-4 display their microstructure morphologies. The SEM images of RFG-1 (Figure 3c) and RFG-3 (Figure 3d) exhibit the highly interconnected, 3D continuous macropore networks. The macropore sizes are concentrated around 100−150 nm. The carbon framework composes of the robust carbon branches with the diameter of ca. 100−200 nm. This indicates the polymer phase has homogeneously separated from the solvent completely and further reveals the complex of GLU and ferric iron as phase separation inducer is effective during the current process. The interconnected macroporosity resulted from spinodal decomposition has already formed during the polymerization process. The SEM images of RFG-4 (Figure 3e,f) show its framework consists of fused carbon spheres with the size ca. 400 nm. The fully interconnected, sponge-like architectures composed of tight packing spherical carbons may serve as buffers against volume variation during lithium-ion insertion and extraction. The gel skeleton and macroporous channels of the products are strongly governed by the dynamics which are driven by the interfacial energy of a sol−gel system. Both the onset of polymerization-induced phase separation and sol−gel transition may change the dynamics of the polymerization systems.[42] The change of the solvent water to polymer ratio is one effective strategy to control the timing of the onset of phase separation relative to the sol−gel transition. When the amount of H$_2$O is high (e.g., the sample prepared using 13.09 mL H$_2$O, see Figure S2), the phase separation takes place much earlier than the gelation, and the polymeric fragments fuse into spherical particles to reduce the interfacial energy. With decreased amount of H$_2$O (RFG-4), the phase separation moves faster, approaching that of the sol−gel transition. Further decreasing the amount of H$_2$O, the onset of sol−gel transition matches well with phase-separation process, ending with finely bicontinuous structure (3.79 mL of H$_2$O for the sample shown in Figure S3; 1.93 mL of H$_2$O for RFG-1).

Electrochemical Performance of the Carbon Nanostructures as Anodes in LIBs. The aforementioned characterization results verify that the current synthesis is effective and facile to produce carbon materials with controlled crystalline pore walls and fully interconnected multimodal pore systems. Considering these attractive features, the carbons as anodes were evaluated in terms of capacities as well as rate performance for the LIBs. The electrochemical data of these carbons are shown in Figure 4. The first galvanostatic charge/discharge profiles of RFG-1 to RFG-4 are exhibited in Figure 4a from 0.005 to 3 V at a current density of 100 mA g^{-1}. As can be seen, the most crystalline RFG-1 and the most amorphous RFG-3 with the less developed porosity deliver the initial discharge capacities of 591 and 803 mA h g^{-1}, respectively. On the other hand, RFG-2 with the most developed porosity gives the largest initial discharge capacity (978 mA h g^{-1}), and close
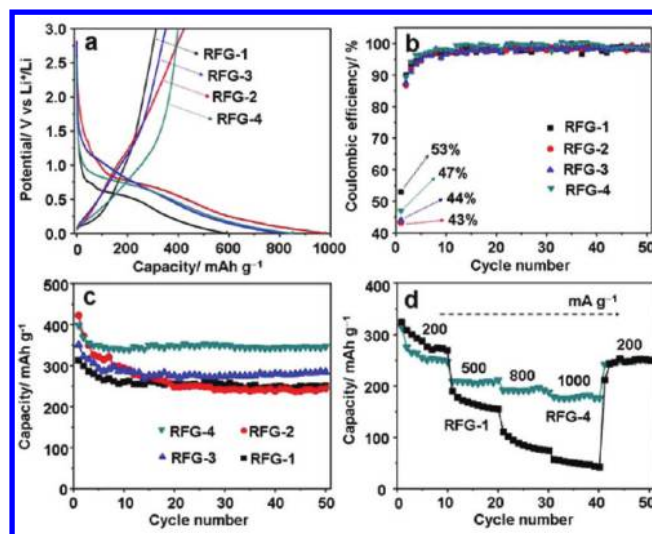

Figure 4. Electrochemical performance of RFG-1, RFG-2, RFG-3, and RFG-4: (a) the first charge/discharge profiles at a current density of 100 mA g^{-1}; (b) Coulombic efficiencies; (c) cycle performance in the range of 0.005−3 V; and (d) rate performance over multiple current densities.

behind is RFG-4 with mixed features of both amorphous and graphitic carbon (851 mA h g^{-1}), indicating the enhanced lithium-ion storage capacity for the rich porosity and high surface area. An initial charge capacity of RFG-2 reaches 421 mA h g^{-1}, which is higher than that of RFG-1 (313 mA h g^{-1}), RFG-3 (353 mA h g^{-1}), and RFG-4 (400 mA h g^{-1}).

However, the calculated initial Coulombic efficiency of RFG-2 is the lowest, with the value of 43%, among these samples (Figure 4b), followed by RFG-3 (44%), RFG-4 (47%), and RFG-1 (53%). Under similar conditions, the initial efficiencies of these carbons are in the same or higher level than that of reference carbonaceous materials (see Figure 5a). The large initial irreversible capacity also occurs in these carbon, especially for RFG-2 (high up to 557 mA h g^{-1}), which is an expected phenomenon in carbonaceous electrodes. Its loss stems from the decomposition of electrolyte that results in the formation of a solid electrolyte interphase (SEI) on the material surface and from the reaction of Li with active sites such as the vicinity of residual H atoms in the electrode.[43] Thus, higher specific surface areas and amorphous structures with various active sites provide much more active sites for the irreversible reaction with lithium ions, leading to larger irreversible capacity. The Coulombic efficiency of these carbon nanostructures increases significantly along with discharge−charge cycles, reaching over 99% when discharge−charged for about five cycles. Obviously, carbon materials having improved crystalline structure are necessary for a high initial efficiency, while the excess micropores are detrimental to the accumulation of reversible capacities. According to past experience,[10] the defective vacancies, boundaries, edges, and corners as well as the H-terminated edges of hexagonal carbon fragments in the micropore systems contribute the most to the accommodation of the excess Li ions. Inevitably, these highly active sites allow a really slow Li diffusion kinetic in the lithium-ion deintercalation process and thus a high irreversible capacity.

The cycling stability during the Li-ion insertion/extraction processes is also a key factor for successful industrial production as anode electrodes. Figure 4c presents the charge cycling performance of these samples for 50 cycles at a current density
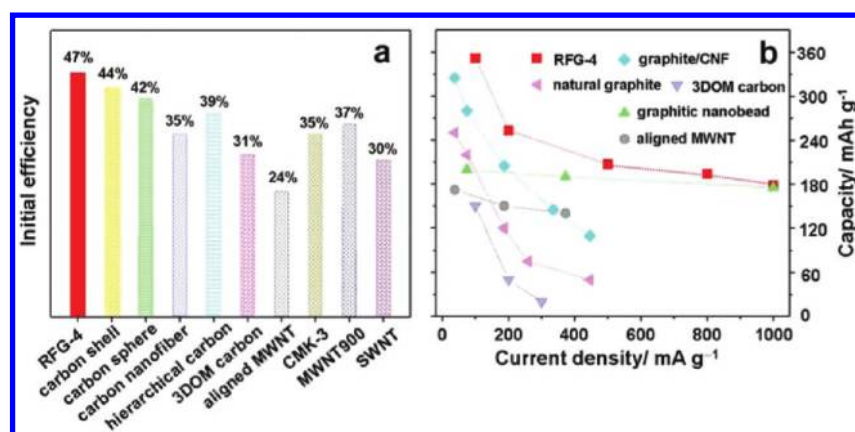
Figure 5. Initial efficiency (a) and rate performance (b) of RFG-4 in this work compared with that of other carbonaceous materials including interconnected hollow graphitic carbon shell (carbon shell),[46] nanographene-constructed hollow carbon sphere (carbon sphere),[47] carbon nanofiber,[48] hierarchical porous carbon (hierarchical carbon),[49] three-dimensionally ordered macroporous carbon (3DOM carbon),[20] aligned multiwall carbon nanotube (aligned MWNT),[50] ordered mesoporous carbon (CMK-3)[51] multiwall carbon nanotube obtained through catalytic decomposition of acetylene at 900 °C (MWNT900)[52] and single-walled carbon nanotube (SWNT),[53] natural graphite, natural graphite-carbon nanofiber composite (graphite/CNF),[54] and graphitized carbon nanobeads (graphitic nanobead).[55] The detailed experimental conditions of the samples used for comparison are listed in Table S1 of the Supporting Information.
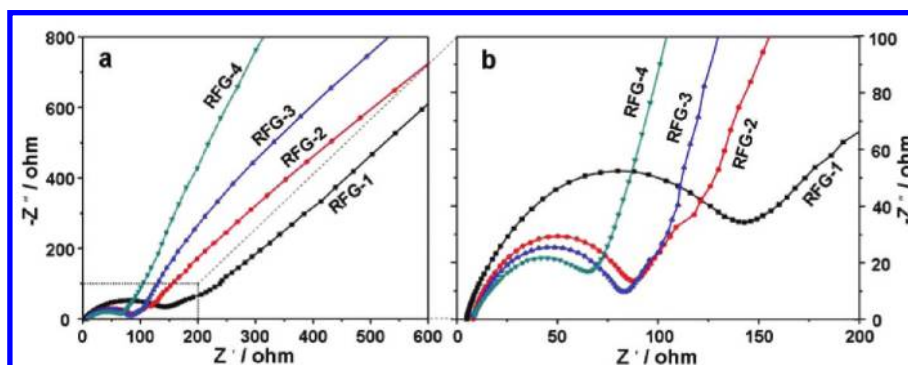

Figure 6. (a) Nyquist plots of these carbon nanostructure anodes in the frequency range of 100 kHz to 0.01 Hz. (b) Close-up of Nyquist plots at high frequency.

of 100 mA g^{-1}. In contrast to the severe decrease in reversible capacity during following cycles of different carbon materials,[44] the four carbon electrodes display stable cycling performance. After 50 cycles, RFG-1, RFG-2, and RFG-3 demonstrated a reversible capacity of 251, 250, and 280 mA h g^{-1}, respectively. After cycles, RFG-4 delivers a significant reversible capacity of 352 mA h g^{-1}, which is higher than that of RFG-1 to RFG-3, and the reported carbonaceous materials.[20,49,54,55] The improvements of RFG-4 can be ascribed to the optimized crystallinity and nanostructure related to highly interconnected carbon framework with moderate crystalline degree and hierarchical pore channels. The reversible capacity is one of the key parameters for fabricating practical anodes. In a full Li-ion battery, if the stabilized capacity (Coulombic efficiency) of the anode material after the first few cycles is not stable, the lithium ions provided by the cathode will be continuously consumed, which, in turn, causes a more rapid capacity fading.

Figure 4d shows the rate performance of RFG-1 and RFG-4 electrodes. The cells were first cycled at 200 mA g^{-1} for 10 cycles, followed by cycling at current densities increasing stepwise to as high as 1000 mA g^{-1}. When a current of 200 mA g^{-1} is applied, a specific discharge capacity of ca. 270 and 250 mA h g^{-1} is obtained for RFG-1 and RFG-4, respectively. The commercial natural graphite, under similar condition (167 mA g^{-1}), remains less than 50 mAh g^{-1}.[49] When the current density

is increased to 1000 mA g^{-1}, RFG-4 can even deliver a stable and high capacity of ~178 mA h g^{-1}, while the corresponding value for RFG-1 is only 44 mA h g^{-1}. Remarkably, when the current density is again set back to 200 mA g^{-1} after even 50 cycles, a stable high capacity of 253 mA h g^{-1} can be resumed in RFG-4.

To analyze the status of electrochemical performance of RFG-4, we further compare its initial efficiency and reverse capacities (rate performance) with that of other reported carbonaceous materials at current densities of 100, 200, 500, 800, and 1000 mA g^{-1}. As shown in Figure 5a,b, RFG-4 with developed porosity and moderate graphitization features are comparable, even better than those of reference samples in term of both of the two parameters under similar conditions. Its superior rate and cycle performance may be attributed to its unique hierarchical pore structure and developed porosities that allow a high electrode/electrolyte interfaces and thus favors the charge-transfer reactions. Besides the endowed developed textures, a moderate crystallinity, i.e., a proper size of L_c and L_a, is desired for lithium-ion transport in the carbon host. Persson and co-workers have demonstrated that lithium-ion diffusivity in graphite is a function of transport direction by both the experimental findings and the first principles calculations.[45] The Li-ion diffusion between graphene planes (ca. $10^{-7}-10^{-6}$ cm^2 s^{-1}) is several orders of magnitude faster
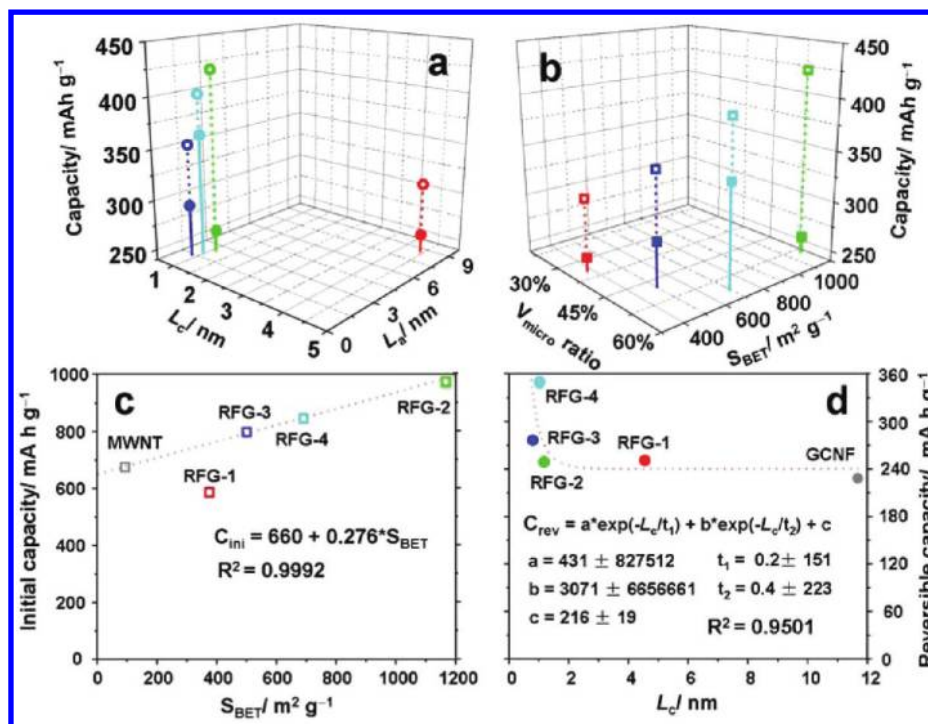
Figure 7. (a) Correlation between the capacity (initial discharging, C_{ini}, and reversible capacity, C_{rev}) and crystalline parameters (L_a and L_c), (b) correlation between the capacity (C_{ini} and C_{rev}) and textural parameters (V_{micro}/V_{total} ratio and S_{BET}), (c) the relationship between S_{BET} and the initial discharging capacity, and (d) the relationship between L_c and reversible capacity after 50 cycles. The hollow symbols represent the initial discharging capacity, while their corresponding solid symbols indicate the reversible capacities after 50 cycles. To better establish the relationship in (c, d), we used the reported data of graphitic carbonaceous samples including interconnected short multiwalled carbon nanotubes (MWNT) and graphitized carbon nanofibers (GCNF) with certain textural parameter and graphitization degree.[8] In (c), the Li-ion storage of RFG-1 is hardly reaching equilibrium in short time at the current density of 100 mA g^{-1} due to its less porosity and most crystalline feature, so its data are not including in this linear fitting.

than that along the grain boundaries or in the direction perpendicular to the graphene layers (ca. 10^{-11} cm^2 s^{-1}). Differing from the graphite with perfect crystalline features (L_a > 100 nm), our graphitic carbon nanostructures contain a variety of nanosized graphitic domains with much smaller crystallite size in a-axis direction (L_a). In this case, the rate limiting process is controlled by the lithium-ion diffusion in the c-axis direction; in other words, a shorter L_c is expected to deliver a rapid lithium-ion diffusion rate in the carbon matrix. In agreement with Persson's findings, our RFG-4 with L_c of 1.0 nm displays more superior rate performance than others with larger L_c in this work and in literatures mentioned above.

To further understand the good rate performance of these carbon materials, the electrochemical impedance spectra (EIS) measurements were conducted to verify the kinetics of Li-ion insertion. As seen in Figure 6a,b, the Nyquist plots are similar to each other in shape, with one depressed semicircle at higher frequency and an inclined line at lower frequency. Generally, the semicircle at high/medium frequency is attributed to the summation of contact resistance, i.e., the SEI resistance and the charge-transfer resistance, while the inclined line at a ca. 45° angle to the real axis is usually assigned to the lithium diffusion process within carbon electrodes.[56,57] It should be pointed out that the intercalation and deintercalation of the lithium ions is usually determined by the charge-transfer resistance.[58] Apparently, RFG-4 with mixed feature of both graphitic and amorphous carbon shows the smallest semicircle diameter, followed by RFG-3 and RFG-2, and RFG-1 with least developed porosity and well graphitic carbon feature gives the largest semicircle diameter. This reveals that the charge transfer

impedance increases in the order RFG-4 < RFG-3 ≈ RFG-2 < RFG-1, indicating that RFG-4 possesses the fastest Li-ion insertion kinetics, though its electrical conductivity is inferior to that of RFG-1. These results further confirmed that the combination of a suitable electronic conductivity, hierarchically interconnected pore system and high surface area provides favorable electron and ion channels for electrochemical reactions, which allow such an excellent high-rate capability for Li-ion insertion and extraction.

From the aforementioned results, it seems that the three most important performance parameters, namely, lithium-ion storage capacity, rate performance, and cycle stability, are strongly dependent on the crystalline characteristics and the porous structures of the carbon electrode materials. As a summary, we proposed the associations between the (ir)-reversible capacity and the pore features, which are shown in Figure 7a,b. As can be seen, RFG-1 with the best graphitic characteristics show the highest initial efficiency; RFG-2 with the most developed porosity, especially the microporosity, delivers the highest initial charge/discharge capacity but the lowest reversible capacities; RFG-3 with significant amorphous features and low surface areas gives a moderate capacity and rate performance; RFG-4 with a moderate crystallinity and relatively developed textural properties shows the best reversible capacity and rate performance. The distinct performance of the RFG-2 further reveals that the graphitic domains of its parent carbon nanostructure (RFG-1 with L_c and L_a of 4.5 and 8.3 nm) have been intensively damaged during the steam activation process accompanied by the formation of more topological defects (micropores, boundaries, corners, and the

H-terminated edges). These defects prefer the Li-ion intercalation, giving the highest lithium storage capacity, but worsen their deintercalation.

As shown in Figure 7c, a well-fitted linear relationship between the initial discharging capacity (C_{ini}) and the specific surface area (S_{BET}) can be obtained by fitting the experimental C_{ini} and S_{BET}. This again confirmed that the large surface areas are favorable for lithium-ion storage capacity due to the rich active sites mentioned above. For the reversible capacity, another possibility arises. For example, RFG-4 with the moderate surface area however shows the largest C_{rev}. Considering the rate-limiting process (Li-ion diffusion along L_c), a well-fitted exponential decay function between the crystallite size in c-axis direction L_c and the reversible capacities after 50 cycles (C_{rev}) was established by using experimental data of C_{rev} and the calculated L_c with the second-order exponential decay fitting (Figure 7d). As expected, the performances of other graphitic nanostructures under similar conditions, such as the thin two-dimensional graphene, also follow this trend. For example, the graphene sheets (<1 nm in c-axis direction) assembled hierarchical nanostructures deliver a high reversible capacity with value up to 1150 mA h g^{-1} after 50 cycles at a current density of 50 mA g^{-1}.[59] To sum up, the high-performance of RFG-4 reveals that a matching of the crystalline degree and porous structure would allows optimized reversible capacity and rate performance. Such reasonable compromise of the two key parameters allows internal Li-ion transport is close to that of the electrons in the external circuit, ending with an optimized electrochemical performance.

Although the crystallinity and porous structure were considered with emphasis, we also discussed the influence of the surface functional groups on the electrochemical performance of anode materials. As mentioned in the Introduction, in order to establish the association on a comparable basis, it is better to use control samples that are derived from the same precursors and under similar procedures. Therefore, we prepared the series of samples using the same polymerization systems with the aim to avoid factors such as heteroatoms and surface chemistry to a great extent. Based on the results of Boehm titration and the elemental analysis listed in Table 1, the proportion of the surface oxygen atom in RFG-2 (the steam activated sample) was calculated to be ~27.8%, which is significantly higher than the other three primitive samples. The capacity of RFG-2 also decreased more rapidly than the other three samples (Figure 4c). Thus, the oxygen-containing functional groups may partially contribute to the decrease in the irreversible capacity. Combining with the above discussions and the fact that RFG-1 shows similar porous structure but better crystallinity and higher surface oxygen density than that of RFG-3, we thus presumably deduce that higher reversible capacity of RFG-1 is mainly contributed from the better crystallinity.

CONCLUSION

Hierarchically multimodal (micro-, meso-/macro-) porous carbons with tunable crystallinity and porosity have been prepared by our simple and effective way through a dual phase separation process and subsequent pyrolysis. Because of their structure features, these carbon materials are tested as anode in LIB. The relationship between the electrochemical performance and the structural features are well established. The integration of both graphitic and amorphous carbon pore walls, moderate accessible surface areas, and highly interconnected pore channels allow the three most important parameters in term of rate performance, cycle stability, and lithium-ion storage capacity in a leading rank among the similar carbonaceous materials. The superior performance is attributed to the highly interconnected carbon framework with moderate crystalline degree and hierarchical pore channels, which ensure a free-resistance lithium-ion transport and fast electron transfer network. More importantly, the correlation between the electrochemical performances and their structural features of crystalline and textural parameters has been established, which may be of great valid for better understanding of the rate performance and cycle stability.

■ ASSOCIATED CONTENT

Ⓢ Supporting Information

Experimental details for test of carbon electrodes; Boehm titration details and results; Raman spectra detected using 532 nm line of laser; SEM image for the sample prepared with different mass ratio; FT-IR spectroscopy and TG curves for RFG-1 to RFG-4. This material is available free of charge via the Internet at http://pubs.acs.org.

■ AUTHOR INFORMATION

Corresponding Author

*E-mail: wencuili@dlut.edu.cn (W.-C.L.); anhuilu@dlut.edu.cn (A.-H.L.).

Notes

The authors declare no competing financial interest.

■ ACKNOWLEDGMENTS

■ REFERENCES

(1) Winter, M.; Brodd, R. J. Chem. Rev. **2004**, 104, 4245−4269.

(2) Endo, M.; Kim, C.; Nishimura, K.; Fujino, T.; Miyashita, K. Carbon **2000**, 38, 183−197.

(3) Guo, Y.-G.; Hu, J.-S.; Wan, L.-J. Adv. Mater. **2008**, 20, 2878−2887.

(4) Tarascon, J.-M.; Armand, M. Nature **2001**, 414, 359−367.

(5) Goodenough, J. B.; Kim, Y. Chem. Mater. **2010**, 22, 587−603.

(6) Etacheri, V.; Marom, R.; Elazari, R.; Salitra, G.; Aurbach, D. Energy Environ. Sci. **2011**, 4, 3243−3262.

(7) Cheng, F.; Tao, Z.; Liang, J.; Chen, J. Chem. Mater. **2008**, 20, 667−681.

(8) Arrebola, J. C.; Caballero, A.; Hernán, L.; Morales, J. J. Electrochem. Soc. **2009**, 156, A986−A992.

(9) Jeong, G.; Kim, Y.-U.; Kim, H.; Kim, Y.-J.; Sohn, H.-J. Energy Environ. Sci. **2011**, 4, 1986−2002.

(10) Kaskhedikar, N. A.; Maier, J. Adv. Mater. **2009**, 21, 2664−2680.

(11) Ji, L.; Lin, Z.; Alcoutlabi, M.; Zhang, X. Energy Environ. Sci. **2011**, 4, 2682−2699.

(12) Hanzawa, Y.; Hatori, H.; Yoshizawa, N.; Yamada, Y. Carbon **2002**, 40, 575−581.

(13) Liang, M.; Zhi, L. J. Mater. Chem. **2009**, 19, 5871−5878.

(14) Wu, Y. P.; Rahm, E.; Holze, R. J. Power Sources **2003**, 114, 228−236.

(15) Su, F.; Zhao, X. S.; Wang, Y.; Zeng, J.; Zhou, Z.; Lee, J. Y. J. Phys. Chem. B **2005**, 109, 20200−20206.

(16) Rolison, D. R.; Long, J. W.; Lytle, J. C.; Fischer, A. E.; Rhodes, C. P.; McEvoy, T. M.; Bourg, M. E.; Lubers, A. M. *Chem. Soc. Rev.* **2009**, *38*, 226−252.

(17) Fang, B.; Kim, M.-S.; Kim, J. H.; Lim, S.; Yu, J.-S. *J. Mater. Chem.* **2010**, *20*, 10253−10259.

(18) Yi, J.; Li, X. P.; Hu, S. J.; Li, W. S.; Zhou, L.; Xua, M. Q.; Lei, J. F.; Hao, L. S. *J. Power Sources* **2011**, *196*, 6670−6675.

(19) Zhou, H. S.; Zhu, S. M.; Hibino, M.; Honma, I.; Ichihara, M. *Adv. Mater.* **2003**, *15*, 2107−2111.

(20) Wang, Z.; Li, F.; Ergang, N. S.; Stein, A. *Chem. Mater.* **2006**, *18*, 5543−5553.

(21) Guo, B.; Wang, X.; Fulvio, P. F.; Chi, M.; Mahurin, S. M.; Sun, X.-G.; Dai, S. *Adv. Mater.* **2011**, *23*, 4661−4666.

(22) Hu, Y.-S.; Adelhelm, P.; Smarsly, B. M.; Hore, S.; Antonietti, M.; Maier, J. *Adv. Funct. Mater.* **2007**, *17*, 1873−1878.

(23) Liu, C.; Li, F.; Ma, L.-P.; Cheng, H.-M. *Adv. Mater.* **2010**, *22*, E28−E62.

(24) Bruce, P. G.; Scrosati, B.; Tarascon, J.-M. *Angew. Chem., Int. Ed.* **2008**, *47*, 2930−2946.

(25) McCreery, R. L. *Chem. Rev.* **2008**, *108*, 2646−2687.

(26) Frackowiak, E.; Béguin, F. *Carbon* **2002**, *40*, 1775−1787.

(27) Lu, A.-H.; Li, W.; Matoussevitch, N.; Spliethoff, B.; Bönnemann, H.; Schüth, F. *Chem. Commun.* **2005**, 98−100.

(28) Liang, C.; Dai, S.; Guiochon, G. *Anal. Chem.* **2003**, *75*, 4904−4912.

(29) Gao, W.; Wan, Y.; Dou, Y.; Zhao, D. *Adv. Energy Mater.* **2011**, *1*, 115−123.

(30) Xia, B. Y.; Wang, J. N.; Wang, X. X.; Niu, J. J.; Sheng, Z. M.; Hu, M. R.; Yu, Q. C. *Adv. Funct. Mater.* **2008**, *18*, 1790−1798.

(31) Fulvio, P. F.; Mayes, R. T.; Wang, X.; Mahurin, S. M.; Bauer, J. C.; Presser, V.; McDonough, J.; Gogotsi, Y.; Dai, S. *Adv. Funct. Mater.* **2011**, *21*, 2208−2215.

(32) Reddy, I. M.; Mahoney, A. W. *J. Agric. Food Chem.* **1995**, *43*, 1436−1443.

(33) Hashimoto, H.; Nishiuma, S.; Takada, K.; Nakamura, K.; Ueno, R.; Den, T. *Jpn. J. Appl. Phys.* **1999**, *38*, 4136−4141.

(34) Kyotani, T.; Nagai, T.; Inoue, S.; Tomita, A. *Chem. Mater.* **1997**, *9*, 609−615.

(35) Wang, Z.; Lu, Z.; Huang, Y.; Xue, R.; Huang, X.; Chen, L. *J. Appl. Phys.* **1997**, *82*, 5705−5710.

(36) Franklin, R. E. *Acta Crystallogr.* **1951**, *4*, 253−261.

(37) Warren, B. E. *Phys. Rev.* **1941**, *59*, 693−698.

(38) Biscoe, J.; Warren, B. E. *J. Appl. Phys.* **1942**, *13*, 364−371.

(39) Zou, L.; Huang, B.; Huang, Y.; Huang, Q.; Wang, C. *Mater. Chem. Phys.* **2003**, *82*, 654−662.

(40) Matthews, M. J. *J. Mater. Res.* **1996**, *11*, 3099−3109.

(41) Heise, H. M.; Kuckuk, R.; Ojha, A. K.; Srivastava, A.; Srivastava, V.; Asthana, B. P. *J. Raman Spectrosc.* **2009**, *40*, 344−353.

(42) Nakanishi, K.; Tanaka, N. *Acc. Chem. Res.* **2007**, *40*, 863−873.

(43) Wang, K.; Li, Z.; Wang, Y.; Liu, H.; Chen, J.; Holmes, J.; Zhou, H. *J. Mater. Chem.* **2010**, *20*, 9748−9753.

(44) Bhardwaj, T.; Antic, A.; Pavan, B.; Barone, V.; Fahlman, B. D. *J. Am. Chem. Soc.* **2010**, *132*, 12556−12558.

(45) Persson, K.; Sethuraman, V. A.; Hardwick, L. J.; Hinuma, Y.; Meng, Y. S.; van der Ven, A.; Srinivasan, V.; Kostecki, R.; Ceder, G. *J. Phys. Chem. Lett.* **2010**, *1*, 1176−1180.

(46) Han, F.-D.; Bai, Y.-J.; Liu, R.; Yao, B.; Qi, Y.-X.; Lun, N.; Zhang, J.-X. *Adv. Energy Mater.* **2011**, *1*, 798−801.

(47) Yang, S.; Feng, X.; Zhi, L.; Cao, Q.; Maier, J.; Müllen, K. *Adv. Mater.* **2010**, *22*, 838−842.

(48) Subramanian, V.; Zhu, H.; Wei, B. *J. Phys. Chem. B* **2006**, *110*, 7178−7183.

(49) Yi, J.; Li, X. P.; Hu, S. J.; Li, W. S.; Zhou, L.; Xu, M. Q.; Lei, J. F.; Hao, L. S. *J. Power Sources* **2011**, *196*, 6670−6675.

(50) Masarapu, C.; Subramanian, V.; Zhu, H.; Wei, B. *Adv. Funct. Mater.* **2009**, *19*, 1008−1014.

(51) Zhou, H.; Zhu, S.; Hibino, M.; Honma, I.; Ichihara, M. *Adv. Mater.* **2003**, *15*, 2107−2111.

(52) Frackowiak, E.; Gautier, S.; Gaucher, H.; Bonnamy, S.; Béguin, F. *Carbon* **1999**, *37*, 61−69.

(53) Gao, B.; Bower, C.; Lorentzen, J. D.; Fleming, L.; Kleinhammes, A.; Tang, X. P.; McNeil, L. E.; Wu, Y.; Zhou, O. *Chem. Phys. Lett.* **2000**, *327*, 69−75.

(54) Zhang, H.-L.; Zhang, Y.; Zhang, X.-G.; Li, F.; Liu, C.; Tan, J.; Cheng, H.-M. *Carbon* **2006**, *44*, 2778−2784.

(55) Wang, H.; Abe, T.; Maruyama, S.; Iriyama, Y.; Ogumi, Z.; Yoshikawa, K. *Adv. Mater.* **2005**, *17*, 2857−2860.

(56) Striebel, K. A.; Sakai, E.; Cairns, E. J. *J. Electrochem. Soc.* **2002**, *149*, A61−A68.

(57) Cheng, F.; Wang, H.; Zhu, Z.; Wang, Y.; Zhang, T.; Tao, Z.; Chen, J. *Energy Environ. Sci.* **2011**, *4*, 3668−3675.

(58) Ha, H.-W.; Yun, N. J.; Kim, K. *Electrochim. Acta* **2007**, *52*, 3236−3241.

(59) Yin, S.; Zhang, Y.; Kong, J.; Zou, C.; Li, C. M.; Lu, X.; Ma, J.; Boey, F. Y. C.; Chen, X. *ACS Nano* **2011**, *5*, 3831−3838.